

Article

# Ancient Roman Mortars from *Villa del Capo di Sorrento*: A Multi-Analytical Approach to Define Microstructural and Compositional Features

Concetta Rispoli <sup>1,2,\*</sup> , Renata Esposito <sup>3</sup>, Luigi Guerriero <sup>1</sup>  and Piergiulio Cappelletti <sup>1,2</sup> 

<sup>1</sup> Dipartimento di Scienze della Terra, dell’Ambiente e delle Risorse, Università di Napoli Federico II, Complesso Universitario Monte Sant’Angelo, Ed. L, Via Cintia 26, 80126 Naples, Italy; luigi.guerriero2@unina.it (L.G.); piergiulio.cappelletti@unina.it (P.C.)

<sup>2</sup> Center for Research on Archaeometry and Conservation Science, CRACS, Ed. L, Via Cintia 26, 80126 Naples, Italy

<sup>3</sup> Dipartimento di Studi Umanistici, Università degli Studi di Napoli Federico II, Via Porta di Massa 1, 80133 Naples, Italy; renataesp@libero.it

\* Correspondence: concetta.rispoli@unina.it

**Abstract:** This research provides a characterization of ancient Roman mortars from “*Villa del Capo di Sorrento*” (commonly known as “*Villa di Pollio Felice*” or “*Bagni della Regina Giovanna*”). A deepened analysis of cementitious binding matrix and aggregates was conducted with the aims of determining possible sources of raw materials and the mix recipe, and to evaluate the minerogenetic secondary processes. Twenty samples taken from the *Villa* were investigated by means of a multi-analytical approach, including polarized optical microscopy on thin sections, X-ray powder diffraction, scanning electron microscopy analysis, energy dispersed spectrometry, simultaneous thermal analyses, and mercury intrusion porosimetry. Bedding mortars were made with slaked lime mixed with volcanic materials, whereas coating mortars were made adding to previous recipe as ceramic fragments. All samples were classified as hydraulic mortars. Cementitious binding matrix was characterized by gel-like C-A-S-H, calcite, hydrocalumite, and gypsum, deriving from lime/pozzolan material. Geomaterials used for mortar production had a local origin. Pozzolan materials, such as volcanic fragments, scoriae, pumice, and crystal fragments derived from both pyroclastic rocks of the *Campi Flegrei* district and from rocks of the *Somma-Vesuvio* complex; porosity test suggest that the products related to minerogenetic secondary processes, make mortars more resistant.

**Keywords:** ancient mortars; analytical characterization; Sorrento Peninsula



**Citation:** Rispoli, C.; Esposito, R.; Guerriero, L.; Cappelletti, P. Ancient Roman Mortars from *Villa del Capo di Sorrento*: A Multi-Analytical Approach to Define Microstructural and Compositional Features. *Minerals* **2021**, *11*, 469. <https://doi.org/10.3390/min11050469>

Academic Editors: Daniel Albero Santacreu, José Cristóbal Carvajal López and Adrián Durán Benito

Received: 8 April 2021  
Accepted: 27 April 2021  
Published: 29 April 2021

**Publisher’s Note:** MDPI stays neutral with regard to jurisdictional claims in published maps and institutional affiliations.



**Copyright:** © 2021 by the authors. Licensee MDPI, Basel, Switzerland. This article is an open access article distributed under the terms and conditions of the Creative Commons Attribution (CC BY) license (<https://creativecommons.org/licenses/by/4.0/>).

## 1. Introduction

The Campania region was renowned during ancient times as *Campania felix*, thanks to its climate, beautiful landscapes, and fertile land. For these reasons, the region was among the favorite places to live in Roman times, with highly populated cities and *otium villae* on the coast [1].

Nowadays, the region has plenty of major archeological sites, such as the eternal Vesuvian cities, *Pompeii*, and *Herculaneum*, the *Campi Flegrei*, which were often visited by rich Roman senators because of the natural baths and the stunning *villae maritimae*, found from *Posillipo* to *Punta Campanella* [2].

These sites, like other remarkable examples in the Campania region, are still preserved despite their location in an aggressive environment, such as the seaside, and the impact of waves and weathering, which is why they have been the object of many scientific studies.

The Department of Earth Sciences, Environment, and Resources (DiSTAR), Federico II University of Naples, for more than twenty years has been engaged in the application of mineralogical and petrographic studies of several ancient finds and monuments, especially of Campania region, such as Roman concrete, mortars, and ceramics, e.g., [3–7].

In this study the area of interest is the Sorrento Peninsula, between the village of *Aequa* (near *Vico Equense*) and the far side of the Sorrentine peninsula with its adjoining islets (Figure 1a). A total of 24 ruins have been identified as structures related to *villae maritimae*, commonly dated, based on their building techniques, between Late Republican period (133–21 B.C.) and the start of the 2nd c. A.D. [2]. In particular, we have focused the study on ancient roman mortars of one of the most remarkable *villa maritima* of the Sorrento Peninsula: *Villa del Capo* (commonly known as *Villa di Pollio Felice* or *Bagni della Regina Giovanna*; Figure 1).

Twenty lime-based mortars were carefully selected from different structures of *Villa del Capo* (Figure 1c) with the aim of characterizing them, especially regarding the cementitious binding matrix and aggregates, to determine the provenance of raw materials and mix recipe, improve the knowledge of Roman construction techniques, and study the secondary mineralogical processes affecting the investigated mortars.

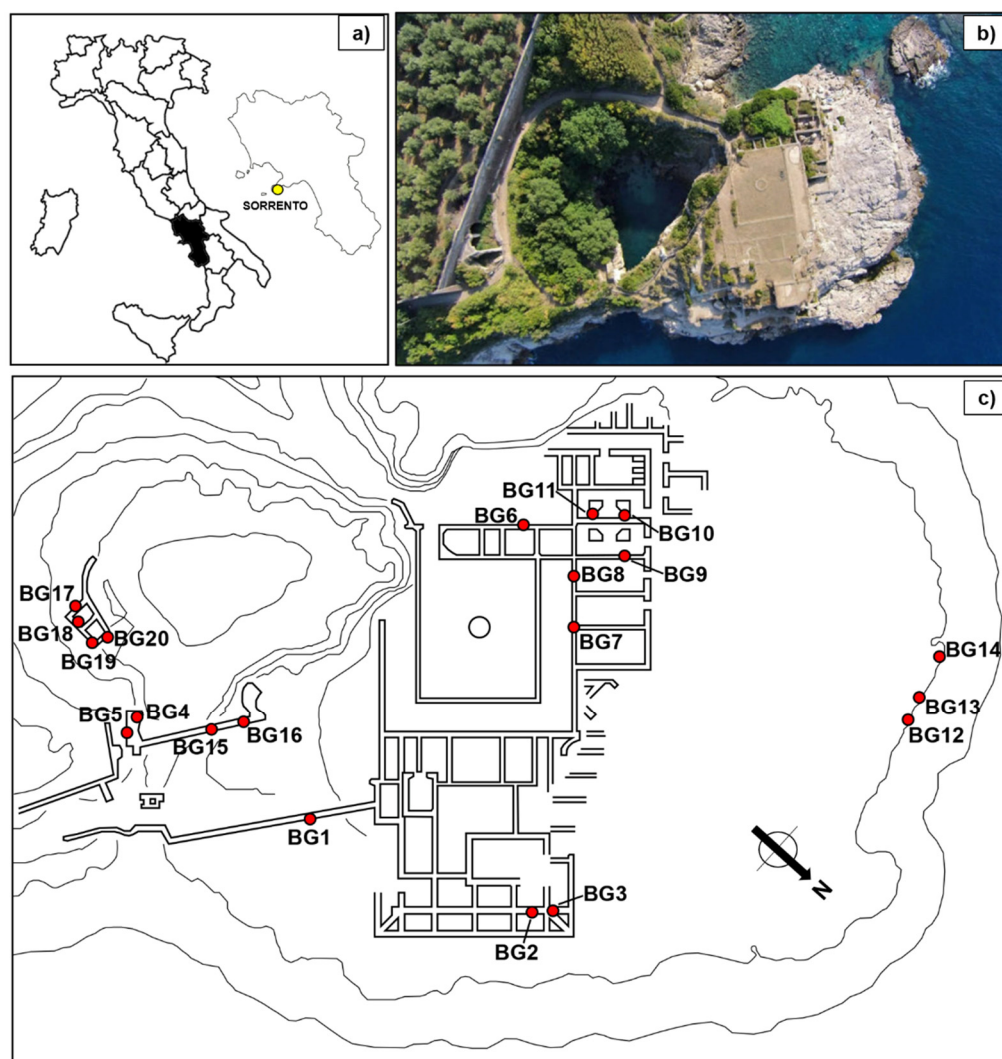


**Figure 1.** (a) Map of Italy and location of Sorrento in the Campania region (Italy); (b) satellite picture of Villa of Capo; (c) sketch map of Villa del Capo with sampling points in red (modified after [8]).

## 2. Geological Context

*Villa del Capo* is located along the northwestern sector of the Sorrento Peninsula at the base of the north facing slope of the Corbo Mt. The ancient building is placed on the distal part of a small promontory that developing in NNW-SSE direction forms the so-called *Punta del Capo*. Being part of the Sorrento Peninsula horst, the Corbo Mt. is formed of Cretaceous

limestones, that widely crop out in the Sorrento Peninsula promontory, overlined by a transgressive Miocene succession, locally covered by quaternary rocks [9] (Figure 2). Forming a morphologic boundary between two semi-grabens located to the north and to the south (i.e., Gulf of Naples and Gulf of Salerno, respectively [9,10] (Figure 2), the Sorrento Peninsula is characterized by a structural setting dominated by NNW-SSE normal faults, resulting from the Plio-Quaternary transcurrent and extensional tectonics [10–12]. Less significant is the structural expression of the Late Miocene–Pliocene compressive tectonics. Similar to the Corbo Mt., the Lattari Mts. Range, forming the Sorrento Peninsula, is consistently mantled by pyroclastic soils representing the product of the activity of the *Somma-Vesuvio* and the *Campi Flegrei*. Such deposits have a thickness ranging from few centimeters to ten meters [12] and were mostly produced by the Holocenic Vesuvius eruption of 79 A.D. Between 18 ka ago and 79 A.D., the Lattari Mts. did not receive any significant fallout deposits, because during this time span, the *Vesuvio* Plinian eruptions were dispersed in other directions (NE to E; [13]). The pyroclastic cover has been subject to both mass wasting and fluvial denudation processes that completely removed it from steeper slopes.

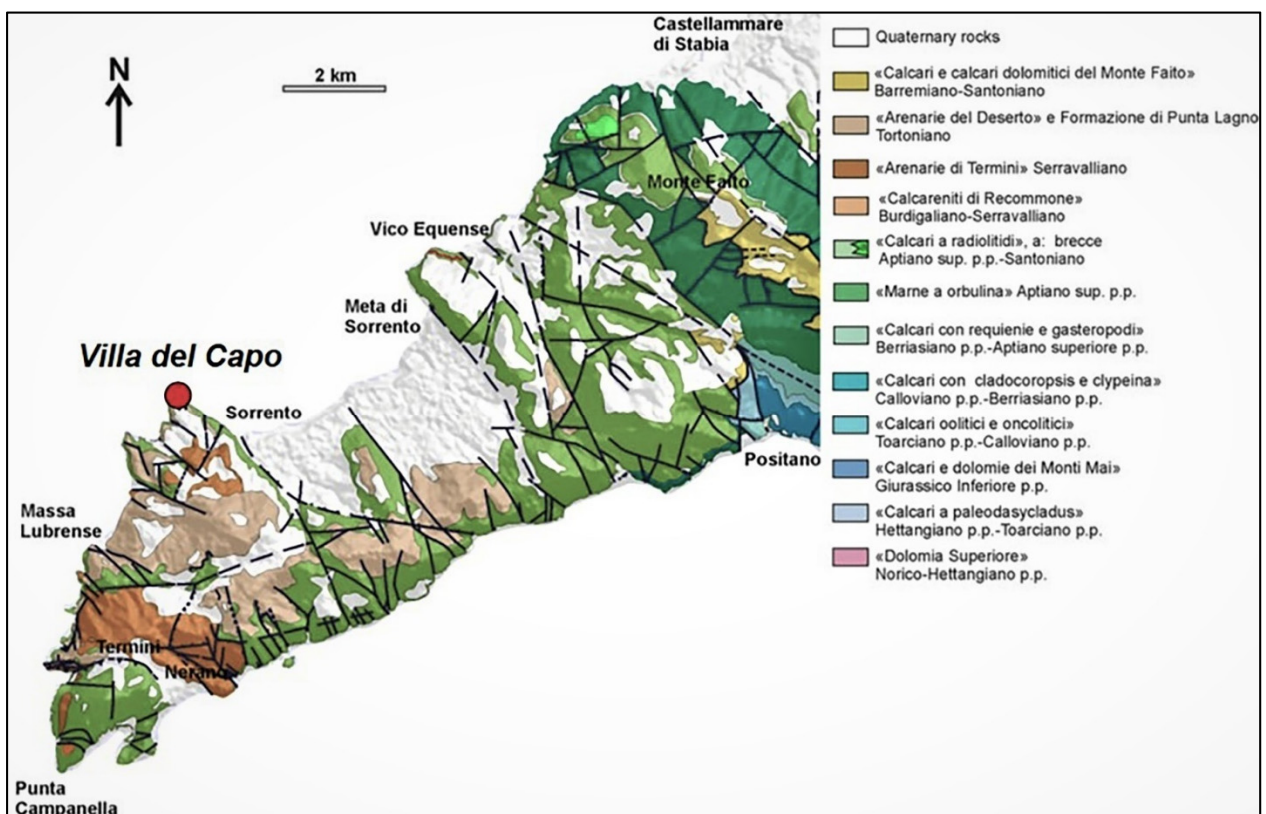


Figure 2. Geological sketch map of the Sorrento Peninsula (modified after [14]).

### 3. The Roman Villa del Capo

Roman *Villa del Capo*, which the popular tradition knew as *I bagni della regina Giovanna* (the baths of Queen Giovanna) or *Villa di Pollio Felice*, was identified by antiquarian tradition, since the sixteenth century, as well as by part of archaeological studies [15]. Located in a unique position, due to the presence of a circular basin, the *villa* is part of a dense network of maritime residences that studded the entire Gulf of Naples between the first century B.C. and the first century A.D. [16].

The Roman residence, organized with different living areas and services, was located on the top of the promontory, and characterized by several continuous terraces along the slope, about 200 m long, down to the sea where there were dockings [15]. The central

area was characterized by four levels with a compact nucleus of buildings; the presence of a peristyle with backyard and central basin on the upper terrace has been documented, where open rooms paved in opus sectile and a system of ramps and stairs linked this place with others. The structures of the *Villa*, facing the Sorrento side, due to the irregularly ascending shape of the area was leveled with the basis of the *Villa* made by *opus caementicium* foundations, exhibiting arches on the first floor and a covered porch with residential rooms at the second one [15]. The thermal area is identified by several rooms near the sea, where traces of their decoration survive, although partially destroyed by sea storms [2]. Finally, *Villa del Capo* continued to be inhabited for several centuries despite the damages caused by *Somma-Vesuvio* eruption of 79 A.D. [16].

#### 4. Materials and Methods

In the context of the ongoing collaboration and related authorization of the former *Soprintendenza archeologia della Campania* and to the assistance of archaeologists, who have carried out several studies on the investigated area, mortar samples were carefully collected in the most representative architectural structures of the archaeological site of *Villa del Capo* (Figure 1c, Table 1).

**Table 1.** Sample list, group, typology, and location.

Sample	Group	Typology	Location
BG1	C	floor mortar	external landing platform
BG2	A	bedding mortar	noble residential area
BG3	A	bedding mortar	noble residential area
BG4	B	coating mortar	bridge and input structures of sea bath
BG5	B	coating mortar	bridge and input structures of sea bath
BG6	A	bedding mortar	<i>quadriportico</i> of sea <i>Villa</i>
BG7	B	coating mortar	cistern of sea <i>Villa</i>
BG8	B	coating mortar	cistern of sea <i>Villa</i>
BG9	C	floor mortar	warehouses
BG10	A	bedding mortar	warehouses
BG11	A	bedding mortar	warehouses
BG12	A	bedding mortar	breakwater
BG13	A	bedding mortar	breakwater
BG14	A	bedding mortar	breakwater
BG15	A	bedding mortar	bridge and input structures of sea bath
BG16	A	bedding mortar	bridge and input structures of sea bath
BG17	B	coating mortar	cistern
BG18	B	coating mortar	cistern
BG19	B	coating mortar	cistern
BG20	B	coating mortar	cistern

The sampling of mortars was preceded by an accurate on-site survey to define the most suitable samples to collect in terms of archaeological and architectural significance. A total of 20 samples was collected comprising ten bedding mortars (Group A), eight coating mortars (Group B) and two floor mortars (Group C).

Samples were removed mechanically with hammers and chisels, ensuring to avoid external and clearly altered portions to study materials that are as close as possible to the original conservation state.

In order to achieve this study's goals, various analytical techniques were used to obtain a mortar's complete petrographic, mineralogical, and chemical characterization and degree of hydraulicity.

The first approach to the study of mortar samples was macroscopic observation, for: (1) identification of the materials and (2) planning of analytical procedures.

Polarized optical microscopy (POM) on polished thin section was performed to observe the textural features and the petrographic composition of the samples with a Leica DFC280 microscope (Leica Camera, Wetzlar, Germany). Percentage of binder and aggregate

was measured via modal analysis on four representative thin sections from each different sector of the investigated area, selected on the base of their macro- and microscopical features. 1500 points for each section were counted using a Leica Q Win image analysis software. Maximum uncertainty of percentage for a total amount of 1500 points is about 2.8% [17].

Qualitative mineralogical analysis was performed by X-Ray Powder Diffraction (XRPD) using a Panalytical X'Pert Pro diffractometer (Malvern PANalytical, Almelo, The Netherlands) equipped with a RTMS X'Celerator detector with Cu-K $\alpha$  radiation, operating at 40 kV and 40 mA. Scans were collected in the range 4–70° 2 $\theta$  using a step interval of 0.017° 2 $\theta$ , with a step counting time of 120 s. Panalytical Highscore Plus 3.0c software (Malvern PANalytical, Almelo, The Netherlands) and PDF-2/ICSD databases were used for identification.

Micro-textural observations and quantitative micro-chemical analyses were carried out by Scanning Electron Microscopy coupled and Energy Dispersive Spectroscopy (SEM/EDS; JEOL JSM-5310 (Jeol Ltd., Tokyo, Japan) coupled with Oxford Instruments Microanalysis Unit, INCA X-act detector (Oxford Instruments plc, Abingdon, Oxfordshire, UK). Measurements were performed with an INCA X-stream pulse processor (ETAS group, Stuttgart, Germany) using a 15-kV primary beam voltage, 50–100  $\mu$ A filament current, variable spot size, from 30,000 to 200,000 $\times$  magnification, 20 mm WD, and 50 s net acquisition real time). The INCA Energy software was employed, using the XPP matrix correction scheme, developed by Pouchou and Pichoir [18], and the Pulse Pile up correction. The quant optimization was carried out using cobalt (FWHM—full width at half maximum peak height—of the strobed zero = 60–65 eV).

Details of the utilized standard and precision and accuracy are provided in [19].

Micro-chemical analyses were performed to determine major chemical composition of binder, lime lumps and aggregates. Hydraulicity index (HI) of binder was calculated according to Boynton using the  $(\text{SiO}_2 + \text{Al}_2\text{O}_3 + \text{Fe}_2\text{O}_3)/(\text{CaO} + \text{MgO})$  ratio.

Thermal Analyses (TGA/SDTA) were carried out with a Mettler Toledo TGA/SDTA 851e instrument (Mettler Toledo, Columbus, OH, USA) and Mettler Toledo STARe SW 7.01 software, with the main goal of determining total (binder plus aggregates) hydraulic features of these materials. Samples were previously dried at 40 °C in a drying oven for 48 h. Thermal analysis was performed within the temperature range of 25–1000 °C, heating rate of 10 °C/min in nitrogen atmosphere (flow 60 mL/min).

Porosity was determined on fragments of mortar (binder and aggregate were not separated) and was evaluated using mercury intrusion porosimetry (MIP), according to ASTM D4404–18 [20]. Due to the scarce amount and small dimensions of samples, on the bases of macroscopic and microscopic features, three fragments were selected, approximately 1 cm<sup>3</sup> in size. Selected fragments were dried in an oven for 24 h at 105 °C, and then analysed on Thermo Scientific equipment PASCAL 140 (ThermoFischer, Waltham, MA, United States) with a maximum injection pressure of 0.4 MPa and PASCAL 240 with a maximum injection pressure of 200 MPa. Total volume of pores of radius between 3.75 nm and 800  $\mu$ m (expressed in mm<sup>3</sup>/g) was determined; open porosity (expressed in vol %); bulk density (g/cm<sup>3</sup>); apparent density (g/cm<sup>3</sup>), and specific surface (m<sup>2</sup>/g); graphical and numerical representation of the distribution of pore sizes were also determined.

## 5. Experimental Results and Discussion

### 5.1. Texture and Optical Microscopy

From a macroscopic point of view, some samples appear to be intact with respect to others that seem to be quite dusty and friable. In addition, they globally show grain size from fine to coarse sand [21]. A brief macroscopic description of mortar Groups (A, B, and C) along with representative sample images is summarized in Table 2.

**Table 2.** List and brief macroscopic description of the examined groups of mortar samples on archaeological site of *Villa del Capo*.

Group	Typology	Binder Color	Aggregate Size	Compactness	Photographic Representation
A (BG15 sample)	Bedding mortars	light grey color	Up to 10 mm	++	
B (BG18 sample)	Coating mortars	Light yellow to reddish	Up to 1.5 cm	+++	
C (BG9 sample)	Floor mortars	pale brown to greyish	Up to 10 mm	+++	

Degree of compactness: +: poor; ++: moderate; +++: high.

Optical microscopy shows that all mortars are characterized by presence of lime lumps (mm to cm). Their formation generally is related to lime binder not well mixed in mortars but sometimes they could be also formed due to not adequate slaking processes of lime or to non-homogeneous temperature in the kiln (under/over-burnt fragments of limestone) [22–24]. Secondary calcite on pore rims and pumice vesicles also occurs.

Binder phase in group A (bedding mortars) is characterized by pale brown/beige to grey color and shows various grades of crystallinity from cryptocrystalline (36.8 Vol.%; Figure 3a) to micritic (22.0 Vol.%; Figure 4b,c). The binder shows the presence of small and fractured lime lumps (5.5 Vol.%, Figure 3b) and few percentages of sparite grains (0.4 Vol.%). Aggregate is mainly composed by volcanic fragments (5.2 Vol.%), pumice (12.0 Vol.%; Figure 3b), and scoriae with clear reaction rims (1.7 Vol.%), mineral aggregates (0.1 Vol.%) formed by clinopyroxene, sanidine, plagioclase, biotite, and, sometimes, calcite, and crystal fragments of sanidine, plagioclase, and clinopyroxene (5.2 Vol.%). Volcanic fragments can be identified as volcanic tuff, characterized by pumice and obsidian fragments, lithics and crystal fragments of sanidine, clinopyroxene, biotite, and plagioclase set in an ashy matrix mainly constituted by volcanic glass shards, affected by secondary mineralization processes [25]. In sample BG12 presence of acicular crystals was also observed, apparently calcite, filling the vugs. (Figure 3c). The binder/aggregate ratio was about 2.7 (Table 3).

Group B (coating mortars) is characterized by a binder that ranges from greyish to brownish color and shows a cryptocrystalline (31.4 Vol.%) and micritic texture (18.9 Vol.%; Figure 3c), small and fractured lime lumps, with not well-defined edges (6.3 Vol.%), and very small percentage of sparite grains (0.4 Vol. %). Aggregate fraction is characterized mainly by ceramic fragments (21.5 Vol.%; Figure 3d–f) with occurrence of reaction rims. Petrographic observations revealed a certain variability in types of ceramic fragments. These sometimes contain temper of different mineralogical composition: for example, in sample BG17 (Figure 3e,f), ceramic fragments containing pumice, scoriae, and small crystals (Figure 3e), and other fragments presenting only crystals of different types (Figure 3f), can be recognized. Moreover, they have also different degrees of porosity and optical activity. The other secondary aggregates that characterize this Group (B) are volcanic and carbonate fragments (2.8 Vol.%–0.5 Vol.%), pumice, and scoriae with reaction rim (4.8 Vol.%; 2.2 Vol.%; Figure 3g) and crystal fragments of plagioclase, sanidine, and clinopyroxene (5.8 Vol.%). Particularly relevant is the presence of leucite-bearing scoriae in BG8 sample (Figure 3h) and the presence of crystal fragments of garnet in BG7 sample (Figure 3i).

Mortars from group B can be identified as *cocciopesto*, a typical building technique used in ancient Rome for waterproof structures, such as cisterns and floors [3,26]. The binder/aggregate ratio is of about 1.5 (Table 3).

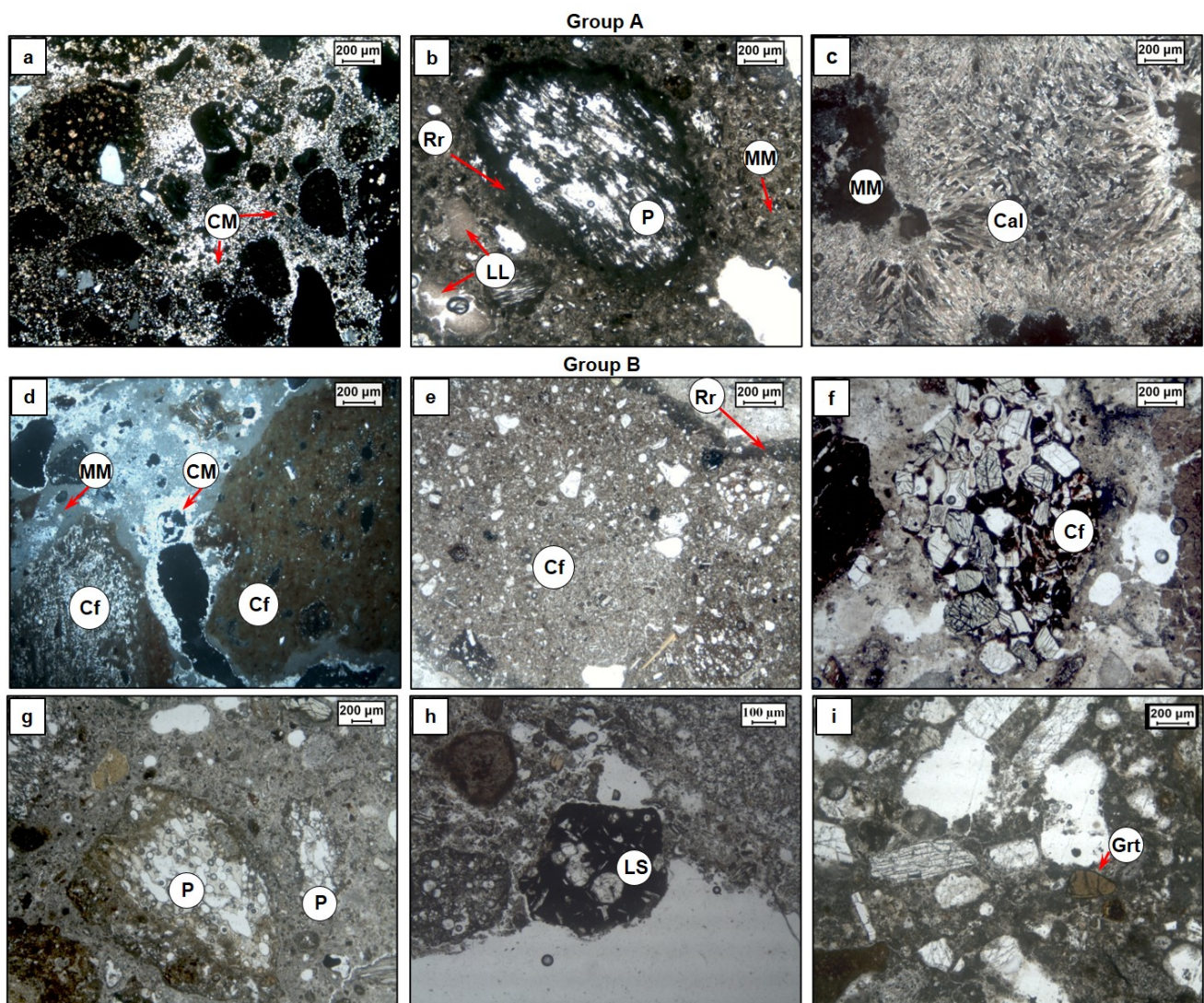


**Figure 3.** Microphotographs of mortar components (in CPL: cross polarized light; PPL: plane polarized light). Abbreviations: MM micritic matrix, CM cryptocrystalline matrix, Rr reaction rim, P pumice, Cf ceramic fragment, Cal calcite, Ls leucite-bearing scoriae, Grt garnet. Group A: (a) cryptocrystalline matrix (CPL) in sample BG3. (b) pumice with reaction rim, lime lumps, and micritic matrix in sample BG6 (PPL). (c) micritic matrix and acicular crystal calcite in sample BG12 (CPL). Group B: (d) cryptocrystalline matrix, micritic matrix, and ceramic fragments in BG19 sample (CPL). (e) ceramic fragment with reaction rim in BG17 sample (CPL). (f) ceramic fragment in BG17 sample (PPL). (g) pumice in BG20 sample (PPL). (h) leucite-bearing scoriae in BG8 sample (PPL). (i) crystal fragment of garnet in BG7 sample.

Floor mortars (Group C) are characterized by two different layers (1 and 0; Figure 4a,b). In BG1 sample, layer 1 (L1, internal layer) is characterized by beige color of binder, with cryptocrystalline to micritic aspect (27.5 Vol.%; 31.3 Vol.%; Figure 4c). Binder also shows presence of small and fractured lime lumps (5.5 Vol.%, Fig; Figure 4c). Aggregates are composed of different types of ceramic fragments (14.1 Vol. %), scoriae (6.2 Vol.%), leucite-bearing scoriae (1.5 Vol.%), and crystal fragments of clinopyroxene, amphibole, plagioclase, sanidine (5.9 Vol. %), and garnet (1.8 Vol.%). Between layers 1 and 0, carbonation processes are evident. (Figure 4d). Modal analysis was performed only in layer 1 and the resulting binder/aggregate ratio was about 2 (Table 3). Layer 0 (external layer) presents a grey color binder and cryptocrystalline aspect (Figure 4d,e). The aggregates are poorly sorted and composed by few leucite-bearing scoriae (Figure 4e), altered pumice, and rare crystal fragments of clinopyroxene.

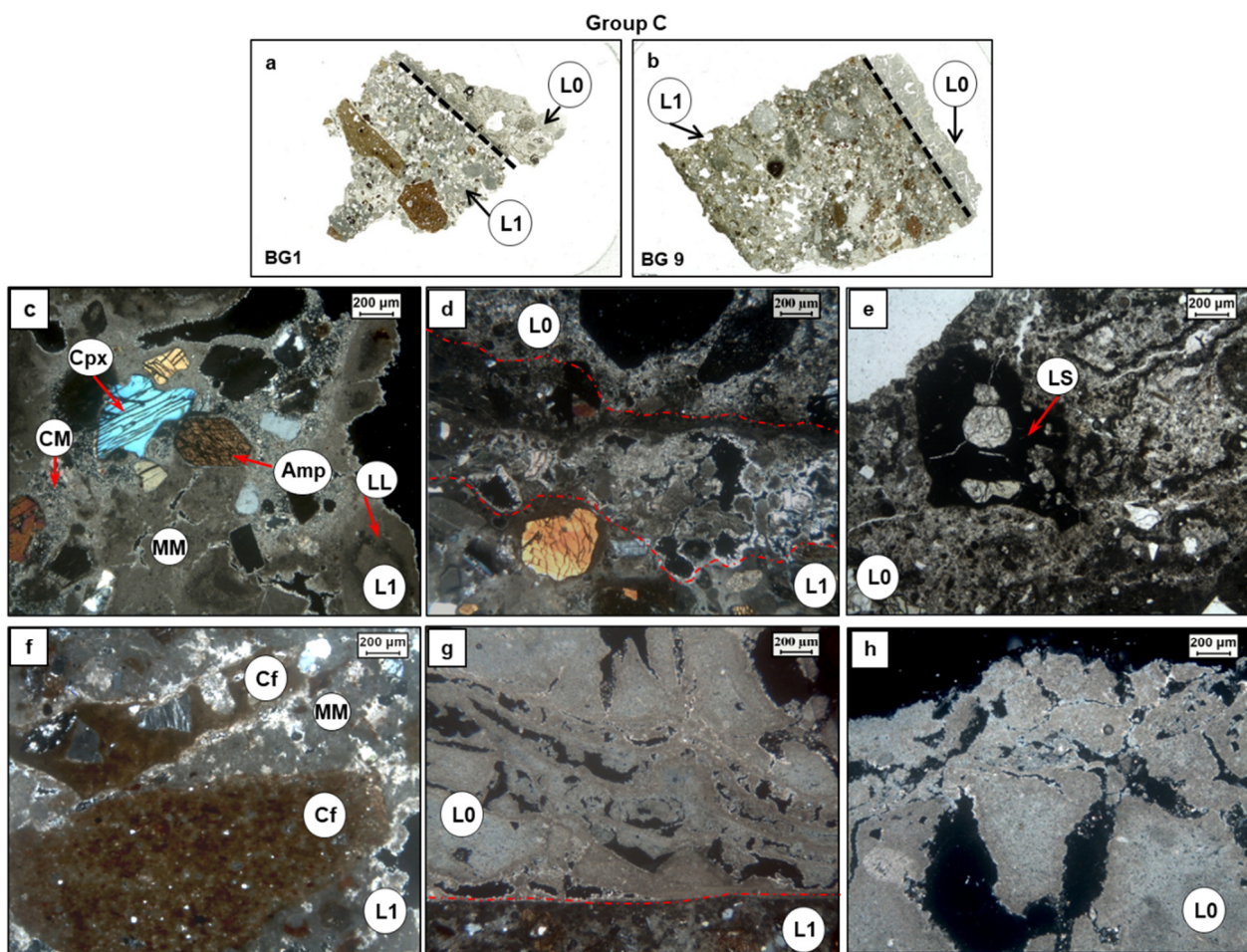


**Figure 4.** Group C: (a) thin section scan of BG1 sample, L1 internal layer, L0 external layer, (b) thin section scan of BG9 sample, L1 internal layer, L0 external layer. (c–h) microphotographs of mortar components (in CPL: cross polarized light; PPL: plane polarized light). Abbreviations: MM micritic matrix, CM cryptocrystalline matrix, Cf ceramic fragment, Ls leucite-bearing scoriae, Cpx clinopyroxene, Amp amphibole. (c) cryptocrystalline matrix, micritic matrix, crystal of amphibole, and clinopyroxene (CPL) in L1 of BG1 sample, (d) transition between L1 and L0 (CPL) in BG1 sample, (e) leucite-bearing scoriae in L0 (PPL) of BG1 sample, (f) micritic matrix and ceramic fragments in L1 of BG9 sample (CPL), (g) transition of L1 and L0 in BG0 sample (CPL), (h) micritic aspect of L0 in BG9 sample (CPL).

In BG9 samples, Layer 1 is characterized by a brownish color of the binder and presents both micritic and cryptocrystalline texture (22.0 Vol.%; 38.0 Vol.%; Figure 4f). Binder phase also shows presence of lime lumps (1.4 Vol.%). Aggregates are composed by different types of ceramic fragments (10.3 Vol.%, Figure 4f), pumice and scoriae with clear reaction rims (10.1 Vol.%–2.9 Vol.%), volcanic fragments (2.1 Vol.%), and crystal fragments (8.2 Vol.%) of clinopyroxene, sanidine, and biotite. Volcanic fragments can be classified as volcanic tuff, characterized by the presence of microcrystals immersed in an altered ashy matrix [8].

Transition between layers 1 and 0 is well defined and evident (Figure 4g). Modal analysis, performed on layer 1, shows binder/aggregate ratio equal to 1.8.

Layer 0 (L0) is characterized by white color of the binder, with mainly micritic aspect with no aggregates (Figure 4h).

**Table 3.** Petrographic features of samples and their modal analysis. Mineral abbreviations from [27].

Mortars	Group A	Group B	Group C (BG1)	Group C (BG9)
<b>Constituents (Vol.%)</b>				
Feldspar (Sa, Pl)	3.7	3.6	4.5	5.3
Mafic Minerals (Cpx, Am, Bt)	1.5	2.2	1.4	2.9
Garnet	-	0.1	1.8	-
Volcanic fragments	5.2	2.8	-	2.1
Scoriae	1.7	2.1	6.2	2.9
Leucite-bearing scoriae	-	0.1	1.5	-
Pumice	12.0	4.8	-	10.1
Ceramic fragments	-	21.5	14.1	10.3
Carbonatic fragments	-	0.5	1.9	-
Sparite	0.4	0.4	0.1	-
Lime lumps	5.5	6.3	3.9	1.4
Micritic matrix	22.0	18.9	31.3	22.0
Cryptocrystalline matrix	36.8	31.4	27.5	38.0
Voids	11.1	2.4	4.7	4.7
Others	0.1	2.9	1.0	0.3
Total points %	100	100	100	100
Total Binder %	64.6	57.1	62.9	61.4
Total Aggregate%	24.1	37.6	31.4	33.7
Binder/Aggregate ratio	2.7	1.5	2.0	1.8

## 5.2. Mineralogy

Samples were separated in (1) binder and (2) aggregates (excluding ceramic fragments, due to their extreme variability) according to the UNI-EN 11305 [28] document (mortar characterization).

XRPD results confirmed occurrence of lime-based mortar with volcanic aggregate, as shown by semi-quantitative analyses reported in Table 4.

Regarding binder phases (Figure 5), calcite is the most abundant phase with subordinate gypsum  $[\text{CaSO}_4 \cdot 2(\text{H}_2\text{O})]$  and hydrocalumite  $\text{Ca}_2\text{Al}(\text{OH})_6[\text{Cl}_{1-x}(\text{OH})_x] \cdot 3(\text{H}_2\text{O})$ . Gypsum, since it is only in a few samples, could be ascribed to sulphation processes of calcite as a consequence of the decrease in pH value, caused by dissolution of atmospheric  $\text{SO}_2$  [29].

Hydrocalumite, also known as Friedel's salt or AFm phase in cement science, belongs to layered double hydroxides (LDHs) family [8,30,31]. LDHs are among the few oxide-based materials with permanent anion exchange capacity, developed through isomorphous substitution [30]. Hydrocalumite has not only an ordered Ca-Al distribution in the hydroxide layer, but well-ordered  $\text{Cl}^-$  and water in the interlayer space. The interlayer order is due to coordination of the water molecules to Ca in the hydroxide layer, which results in an unusual 7-coordinate Ca environment. This phase occurs naturally and generally forms by reaction of Cl-containing de-icing salts with the calcium aluminates of Portland cement [32]. In *Villa del Capo* mortars hydrocalumite is ascribable to the reaction between the  $\text{Ca}(\text{OH})_2$ , sea-water, and hydroxyaluminate derived from pozzolanic materials [31].

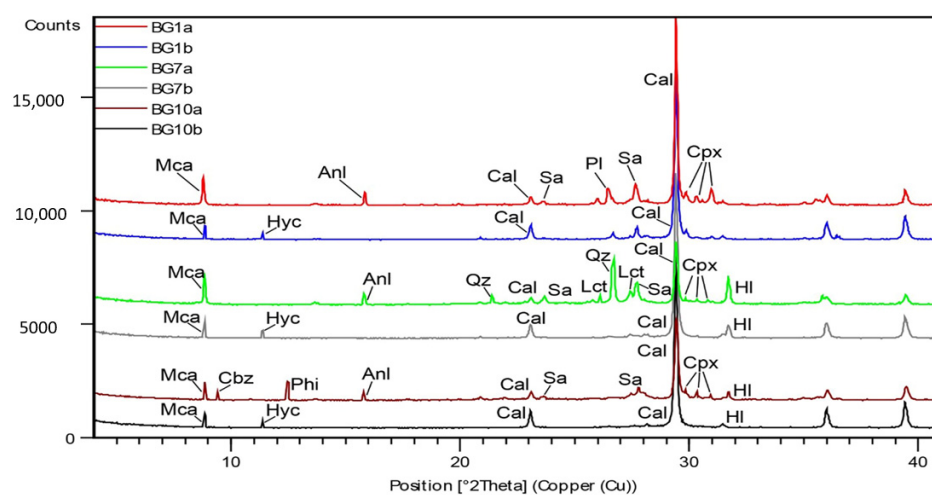
As far as volcanic aggregates fraction is concerned (Figure 5), XRPD analyses suggest that volcanic tuff fragments can be associated to *Campi Flegrei* ignimbrite products (Neapolitan Yellow Tuff and/or Campanian Ignimbrite), due to the presence of typical zeolitic association of this material, i.e., phillipsite, chabazite, and analcime [33,34]. In addition, presence of sanidine, clinopyroxene, and mica could be also associated to the *Campi Flegrei* ignimbrite formations.

All samples show the presence of halite, associated with marine aerosol.

XRPD analysis allowed to detect the presence of amorphous fraction, recognized by the rising of the pattern background, related to volcanic glass components and C-A-S-H (calcium, aluminum, silicate, hydrate) phases.

**Table 4.** Qualitative mineralogical composition of samples, XRPD analysis. Mineral abbreviations from [27].

Samples	Group	Main Binder Phases	Main Aggregates Phase
BG1	C	Cal, Hyc	Anl, Sa, Pl, Cpx, Mca, Cal
BG2	A	Cal, Gp, HI	Anl, Sa, Pl, Mca, HI, Cal
BG3	A	Cal, HI	Phi, Anl, Sa, Pl, Cpx, Mca, HI, Cal
BG4	B	Cal, HI	Phi, Anl, Sa, Pl, Cpx, Mca, Cal
BG5	B	Cal	Phi, Anl, Sa, Pl, Cpx, Mca, Cal
BG6	A	Cal, Hyc, HI	Phi, Pl, Cpx, Mca, HI, Cal
BG7	B	Cal, Hyc, HI	Anl, Pl, Qz, Cpx, Mca, Lct, HI, Cal
BG8	B	Cal, Gp, Hyc, HI	Anl, Sa, Pl, Qtz, Cpx, Lct, Mca, HI, Cal
BG9	C	Cal	Phi, Cbz, Anl, Sa, Pl, Qtz, Cpx, Mca, HI, Cal
BG10	A	Cal, Hyc, HI	Phi, Cbz, Anl, Sa, Pl, Cpx, Mca, HI, Cal
BG11	A	Cal, HI	Phi, Anl, Sa, Pl, Mca, HI, Cal
BG12	A	Cal, Gp, Hyc, HI	Phi, Cbz, Anl, Sa, Pl, Cpx, Mca, HI, Cal
BG13	A	Cal, Gp, Hyc, HI	Phi, Cbz, Anl, San, Pl, Cpx, Mca, HI, Cal
BG14	A	Cal, Hyc, HI	Phi, Anl, Sa, Pl, Cpx, Mca, HI, Cal
BG15	A	Cal, HI	Phi, Anl, Sa, Pl, Cpx, Mca, HI, Cal
BG16	A	Cal, Hyc, HI	Phi, Anl, Sa, Pl, Cpx, Mca, HI, Cal
BG17	B	Cal, Gp	Phi, Anl, Sa, Pl, Cpx, Qz, Mca, Cal
BG18	B	Cal	Phi, Cbz, Anl, Sa, Cpx, Pl, Mca, Cal
BG19	B	Cal	Phi, Cbz, Anl, Sa, Pl, Cpx, Mca, Cal
BG20	B	Cal, Gp	Phi, Anl, Sa, Pl, Cpx, Qz, Mca, Cal

**Figure 5.** XRPD patterns of selected mortars. BG1a: BG1 aggregate fraction (group C); BG1b: BG1 binder fraction (group C); BG7a: BG7 aggregate fraction (group B); BG7b: BG7 binder fraction (group B); BG10a: BG10 aggregate fraction (group A); BG10b: BG10 binder fraction (group A). Mineral abbreviations from [27], Cal calcite, Gp gypsum, Hyc hydrocalumite, Phi phillipsite, Cbz chabazite, Anl analcime, Sa sanidine, Pl plagioclase, Cpx clinopyroxene, Mca mica, Qz quartz, HI halite.

### 5.3. Micro-Morphology and Chemical Analysis (SEM-EDS)

#### 5.3.1. Binder and Lime Lumps

SEM-EDS analysis was carried out to obtain information about the type of lime used to produce the mortars, defining the Hydraulic Index (HI) of the binder and lime lumps.

SEM-EDS analysis of binder showed presence of newly formed hydraulic phases (C-A-S-H), and confirmed, as XRPD suggested, presence of halite and hydrocalumite (Figure 6). Gel C-A-S-H derived from reactions between lime and pozzolanic material (volcanic and ceramic materials). Pozzolanic materials consist predominantly of silica and alumina that are able to combine with slaked lime in the presence of water to produce new reaction products exhibiting a binding character, the so-called CASH phases [35]. Occurrence of hydrocalumite recognized in relict pores of *Villa del Capo* mortars, is associated to the migration of  $\text{Cl}^-$  anions from the sea-water saturated in  $\text{Ca}(\text{OH})_2$  to aluminum-rich sites along the edges of the relict lime clasts or in the voids of mortars [36].

EDS analyses on binder were realized averaging out four measurements for each investigated mortar sample and the results were considered as representative of chemical composition. Based on the mean values of the detected major elements (Table 5), binder results composed by  $\text{CaO} + \text{MgO}$  ranging from a minimum value of 78.31 wt% for sample BG17 to a maximum of 87.11 wt% for BG3 and values of  $\text{SiO}_2 + \text{Al}_2\text{O}_3 + \text{Fe}_2\text{O}_3$  varying from 10.39 wt% for BG1 to 18.77 wt% for BG20.

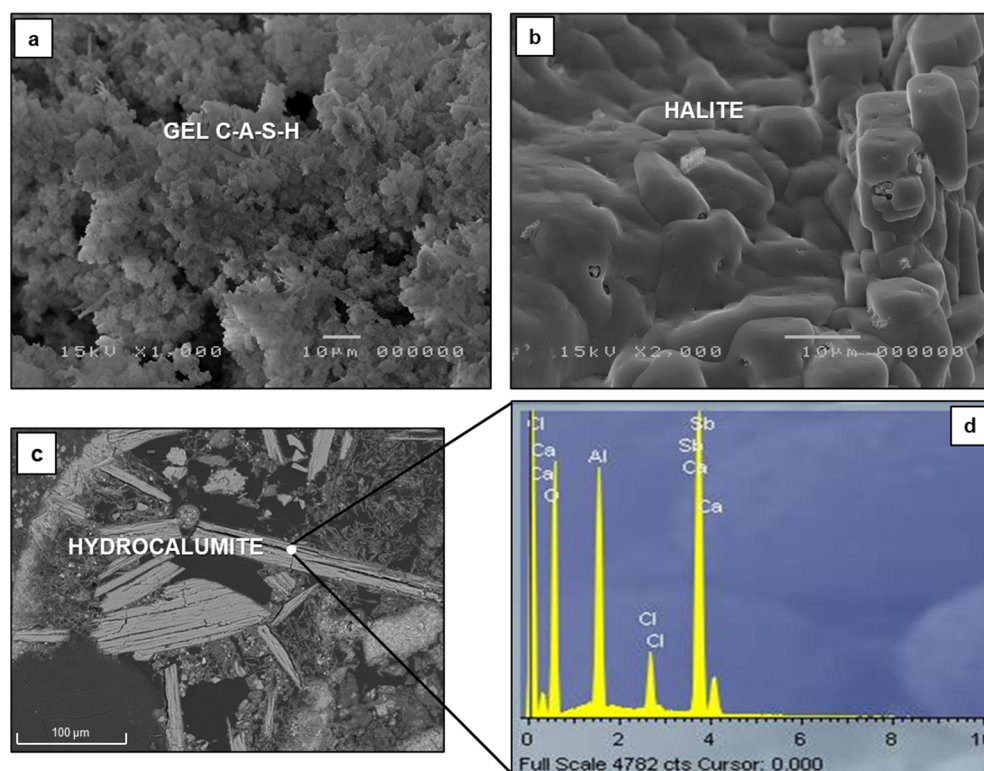


**Figure 6.** SEM images of (a) Gel C-A-S-H, BG17 binder sample; (b) halite crystals, BG10 binder sample; (c) BSE-SEM image of hydrocalumite, BG8 sample; (d) EDS spectrum of hydrocalumite, BG8 sample.

The Hydraulicity Index (HI), calculated according to Boynton's formula [37], showed values ranging between 0.12 and 0.25 wt%; in particular, mortar samples of Group A and C should be considered as weakly hydraulic lime ( $0.10 < \text{HI} < 0.15$  wt%; Figure 7); samples of Group B are moderately hydraulic limes ( $0.16 < \text{HI} < 0.31$  wt%; Figure 7). Regarding the investigation of lime lumps (Table 6), three measurements were performed for each detected lump and performed in their central portion, to reduce the level of contamination. Lime lumps were found to be composed mainly of  $\text{CaO}$ , with very high

values of CaO + MgO ranging from 90.56 wt% (BG9) to a maximum of 96.56 wt% (BG6) and low values of SiO<sub>2</sub> + Al<sub>2</sub>O<sub>3</sub> + Fe<sub>2</sub>O<sub>3</sub> all less than 5 wt%. The Hydraulicity Index related to lime lumps shows values from 0.01 and 0.05 wt% (0.03 < HI < 0.05 wt%; Figure 7), as a result of lumps with aerial properties (H.I. < 0.10). Considering these results, it is possible to infer that mortars became hydraulic by addition of aggregates (volcanic materials and ceramic fragments) with peculiar features. These aggregates, as said previously, produced a “pozzolanic reaction”, due to their silica and alumina content, that reacted with calcium hydroxide leading to the formation of calcium aluminum silicate hydrates, C-A-S-H phases [8,38,39], furtherly testified and confirmed by reaction rims around pumice, scoriae, and ceramic fragment (Figure 3).

**Table 5.** Average values of major oxides (wt%, recalculated to 100%, EDS) of lime lumps (L). SiO<sub>2</sub> + Al<sub>2</sub>O<sub>3</sub> + Fe<sub>2</sub>O<sub>3</sub>, CaO + MgO, HI (hydraulic index) is also shown.

Group	A	A	A	A	A	A	A	A	A	A	B	B	B	B	B	B	B	B	C	C
wt%	BG2 L	BG3 L	BG6 L	BG10 L	BG11 L	BG12 L	BG13 L	BG14 L	BG15 L	BG16 L	BG4 L	BG5 L	BG7 L	BG8 L	BG17 L	BG18 L	BG19 L	BG20 L	BG1 L	BG9 L
SiO <sub>2</sub>	1.95	1.55	1.34	2.87	1.91	1.79	2.34	2.46	1.52	2.14	3.73	1.25	0.52	1.92	1.72	2.88	1.93	2.83	2.34	2.21
TiO <sub>2</sub>	0.12	-	-	-	-	-	0.02	0.13	-	-	0.88	-	-	-	0.34	-	0.24	0.06	-	0.37
Al <sub>2</sub> O <sub>3</sub>	2.02	1.16	1.32	0.86	0.99	1.03	1.19	0.39	1.43	1.54	0.82	2.13	2.43	1.83	2.10	1.08	2.06	1.08	1.32	1.21
Fe <sub>2</sub> O <sub>3</sub>	0.09	0.20	-	0.37	0.38	0.31	-	0.34	0.50	0.10	-	0.37	0.50	0.44	-	0.41	-	0.21	-	-
MnO	-	-	-	-	-	0.12	-	0.09	0.42	0.06	0.15	0.22	0.42	0.32	0.41	0.20	0.42	0.11	-	0.19
MgO	0.56	1.14	1.87	2.48	2.45	0.56	1.87	2.80	0.55	1.73	1.28	0.60	0.55	0.46	2.13	0.26	1.12	0.36	1.87	2.19
CaO	92.78	94.80	94.68	91.12	93.04	94.28	93.80	91.89	93.11	93.61	91.09	94.23	93.11	93.47	92.07	93.36	93.79	93.70	93.68	88.38
Na <sub>2</sub> O	0.42	0.32	0.16	0.45	0.27	0.27	0.16	0.19	0.42	0.17	0.90	0.32	0.42	0.23	0.18	0.59	0.13	0.72	0.16	0.69
K <sub>2</sub> O	0.16	-	-	-	-	-	-	-	-	0.18	0.13	0.09	-	-	0.09	0.55	0.08	0.51	-	0.03
P <sub>2</sub> O <sub>5</sub>	0.05	-	-	-	-	-	-	-	-	-	-	-	-	-	-	-	-	-	-	0.48
BaO	0.49	-	0.49	-	-	0.09	0.49	0.05	-	0.09	0.00	-	-	-	-	-	0.06	-	0.49	-
SO <sub>3</sub>	0.12	0.19	0.13	0.99	0.10	1.13	0.13	0.62	1.16	0.23	0.29	0.44	0.40	0.10	0.02	0.24	-	0.29	0.13	0.30
Cl-	0.89	0.65	-	0.87	0.87	0.23	-	0.87	0.40	0.15	0.30	0.16	1.16	1.04	0.20	0.43	-	0.14	-	3.70
F-	0.34	-	-	-	-	0.18	-	0.16	0.47	0.00	0.42	0.18	0.47	0.18	0.75	-	0.17	-	-	0.25
Total	100.00	100.00	100.00	100.00	100.00	100.00	100.00	100.00	100.00	100.00	100.00	100.00	100.00	100.00	100.00	100.00	100.00	100.00	100.00	100.00
SiO <sub>2</sub> + Al <sub>2</sub> O <sub>3</sub> + Fe <sub>2</sub> O <sub>3</sub>	4.07	2.90	2.67	4.09	3.28	3.13	3.53	3.19	3.46	3.78	4.54	3.76	3.46	4.20	3.82	4.37	3.99	4.12	3.67	3.42
CaO + MgO	93.34	95.94	96.56	93.60	95.49	94.84	95.68	94.69	93.66	95.34	92.37	94.83	93.66	93.93	94.20	93.62	94.91	94.06	95.56	90.56
HI	0.04	0.03	0.03	0.04	0.03	0.03	0.04	0.03	0.04	0.04	0.05	0.04	0.04	0.04	0.04	0.05	0.04	0.04	0.04	0.04

**Table 6.** Average values of major oxides (wt%, recalculated to 100%, EDS) of binder (B). SiO<sub>2</sub> + Al<sub>2</sub>O<sub>3</sub> + Fe<sub>2</sub>O<sub>3</sub>, CaO + MgO, HI (hydraulic index) is also shown.

Group	A	A	A	A	A	A	A	A	A	A	B	B	B	B	B	B	B	B	C	C
wt%	BG2 B	BG3 B	BG6 B	BG10 B	BG11 B	BG12 B	BG13 B	BG14 B	BG15 B	BG16 B	BG4 B	BG5 B	BG7 B	BG8 B	BG17 B	BG18 B	BG19 B	BG20 B	BG1 B	BG9 B
SiO <sub>2</sub>	8.03	8.24	7.76	8.04	8.89	8.34	9.03	9.52	6.79	8.73	9.82	10.76	9.76	10.27	14.11	12.90	13.99	14.32	7.94	8.85
TiO <sub>2</sub>	0.19	0.22	-	0.33	0.13	-	0.05	0.21	-	-	-	-	-	-	0.26	0.24	0.28	0.14	-	0.40
Al <sub>2</sub> O <sub>3</sub>	2.69	2.41	3.07	2.34	2.15	3.76	3.13	2.03	3.77	2.92	3.19	3.27	3.07	2.82	3.70	3.82	3.17	3.59	2.24	2.65
Fe <sub>2</sub> O <sub>3</sub>	0.17	0.25	0.28	0.18	0.11	0.12	0.15	0.02	0.19	0.21	0.70	0.78	0.28	0.20	0.90	1.27	0.35	0.87	0.21	0.00
MnO	-	0.07	0.15	0.17	0.07	-	0.06	0.11	-	0.14	0.09	0.15	0.15	0.10	0.32	0.00	0.44	0.06	0.24	0.48
MgO	0.24	3.92	3.34	4.04	2.94	1.41	2.33	3.67	1.42	3.11	5.19	2.34	3.34	2.73	0.67	7.78	0.80	5.64	0.71	0.74
CaO	85.72	83.18	82.56	83.02	83.83	83.62	82.54	83.02	84.83	82.61	78.61	80.47	80.56	82.06	77.64	71.74	78.62	72.96	85.67	83.58
Na <sub>2</sub> O	0.82	0.68	0.91	0.71	0.45	0.81	0.97	0.71	0.89	0.39	0.86	0.52	0.91	0.72	1.07	0.53	1.06	0.63	1.20	1.37
K <sub>2</sub> O	0.20	0.15	0.22	0.19	0.09	0.24	0.14	0.14	0.43	0.22	0.13	0.22	0.22	0.13	0.74	0.30	0.58	0.40	0.35	0.94
P <sub>2</sub> O <sub>5</sub>	-	0.04	-	0.04	0.04	-	-	-	-	-	0.09	-	-	-	-	-	-	-	0.30	0.30
BaO	0.70	0.07	0.22	0.08	0.06	1.06	0.22	0.08	1.01	0.30	0.00	0.22	0.22	0.08	0.10	-	0.19	0.00	0.27	0.20
SO <sub>3</sub>	0.53	0.23	0.62	0.28	0.56	0.10	0.83	0.21	0.10	0.58	0.52	0.70	0.62	0.42	0.26	0.83	0.26	0.74	0.61	0.50
Cl-	0.21	0.53	0.24	0.58	0.68	0.53	0.15	0.28	0.56	0.19	0.80	0.24	0.24	0.13	0.23	0.60	0.25	0.66	0.26	-
F-	0.48	-	0.63	-	-	-	0.40	-	-	0.59	-	0.33	0.63	0.34	-	-	-	-	-	-
Total	100.00	100.00	100.00	100.00	100.00	100.00	100.00	100.00	100.00	100.00	100.00	100.00	100.00	100.00	100.00	100.00	100.00	100.00	100.00	100.00
SiO <sub>2</sub> + Al <sub>2</sub> O <sub>3</sub> + Fe <sub>2</sub> O <sub>3</sub>	10.89	10.91	11.11	10.57	11.15	12.22	12.31	11.58	10.76	11.87	13.71	14.81	13.11	13.29	18.71	17.99	17.51	18.77	10.39	11.49
CaO + MgO	85.96	87.11	85.89	87.06	86.77	85.03	84.87	86.69	86.25	85.72	83.80	82.81	83.89	84.79	78.31	79.52	79.42	78.60	86.38	84.32
HI	0.13	0.13	0.13	0.12	0.13	0.14	0.14	0.13	0.12	0.14	0.16	0.18	0.16	0.16	0.24	0.23	0.22	0.24	0.12	0.14

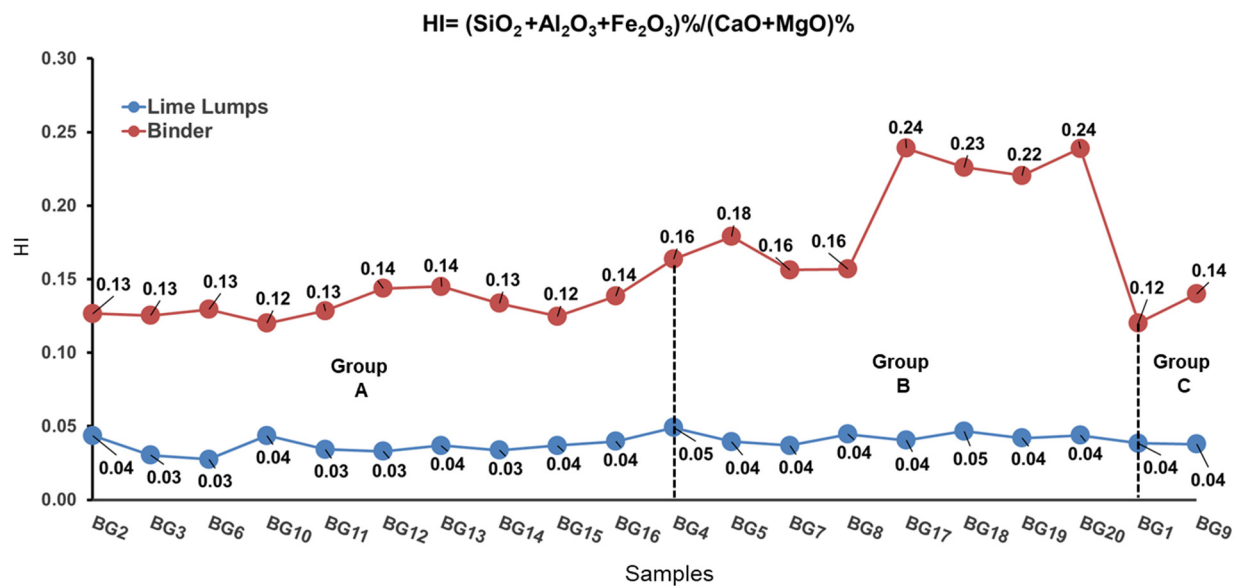


**Figure 7.** Hydraulicity index (HI) for lime lumps (blue line) and binder (red line) of analyzed mortars.

### 5.3.2. Volcanic Aggregates

SEM-EDS analysis of volcanic aggregates were performed to obtain additional information about the provenance of raw materials. Results confirmed the above-mentioned hypothesis of the employment of *Campi Flegrei* tuff aggregates, due to the presence of phillipsite with well-defined prismatic crystal habit and pseudo cubic crystals of chabazite [33].

EDS microanalysis was carried out on pumice from mortar samples (see Supplementary Materials Table S1). Using Total Alkali versus Silica diagram (TAS) for the effusive volcanic rocks [40], it is possible to observe that pumice fragments show trachytic compositions; their classification follows the compositional trend of *Campi Flegrei* products (Figure 8a). Results also suggested the use of geomaterials from the *Somma-Vesuvio* complex, due to the presence of volcanic scoriae containing analcime (typical product of leucite alteration; Figure 8b) and garnet fragments [13] typical of these materials. In support of this hypothesis, chemical composition of analyzed garnet (calculated following [41]; (see Supplementary Materials Table S2) shows similarity with garnets of *Somma-Vesuvio* (andradite 46–70 mol% and grossularia 16–45 mol%; taken by [42]; unpublished data on garnets from intrusive *Somma-Vesuvio* rocks. L. Melluso, personal communication).

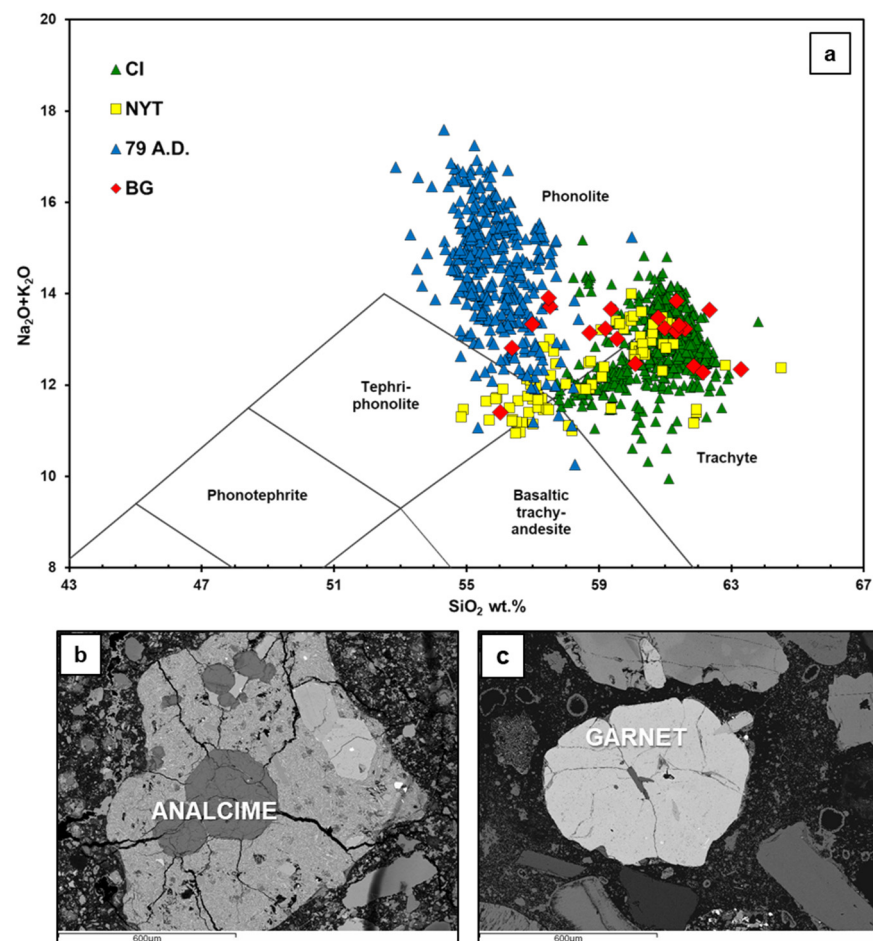


**Figure 8.** (a) Total Alkali Silica (TAS) diagram [40] showing the composition of pumice fragments analyzed in the investigated samples (BG, *Villa del Capo*) and comparison with Phlegraean pumice (CI, Campanian Ignimbrite and NYT, Neapolitan Yellow Tuff; data from [43] and references therein). (b) BSE- SEM images of analcime bearing scoria in BG1 sample, (c) BSE- SEM images of garnet crystal in BG7 sample.

### 5.3.3. Ceramic Aggregates

Regarding ceramic fragments, SEM-EDS analysis allowed to confirm extreme differences occurring between them, even ones from the same mortar sample (Figure 9). These differences are testified by the different mineralogical composition, different texture, different porosity, and by the different chemical composition of matrix.

Chemical analysis on matrix of representative ceramic fragments (Table 7) showed different concentration in CaO ranging from 2.87 wt% for sample BG12 to a maximum of 19.08 wt% for BG4b.

The concentration of this oxide is a strong discriminant of ceramics in relation to their final use. When the percentage of this oxide is less than 6% [44] the clayey raw material used to produce ceramics is defined non calcareous, otherwise it is said calcareous ( $\text{CaO} > 6\%$ ). Non calcareous clays are best suited for making cookware, due to the better thermal shock resistance of the end products, whereas calcareous clays are generally employed to produce pottery used as containers [45].

Differences between ceramic fragments does not allow for defining provenance but represent a testimony of the re-use of ceramic waste materials in preparations of mortars. The relevant role played by ceramic fragments was to provide hydraulicity to the mortars, as pointed out by HI evaluation (Figure 7). Coating and floor mortars that contain both pozzolana and ceramics materials are characterized by highest HI values.

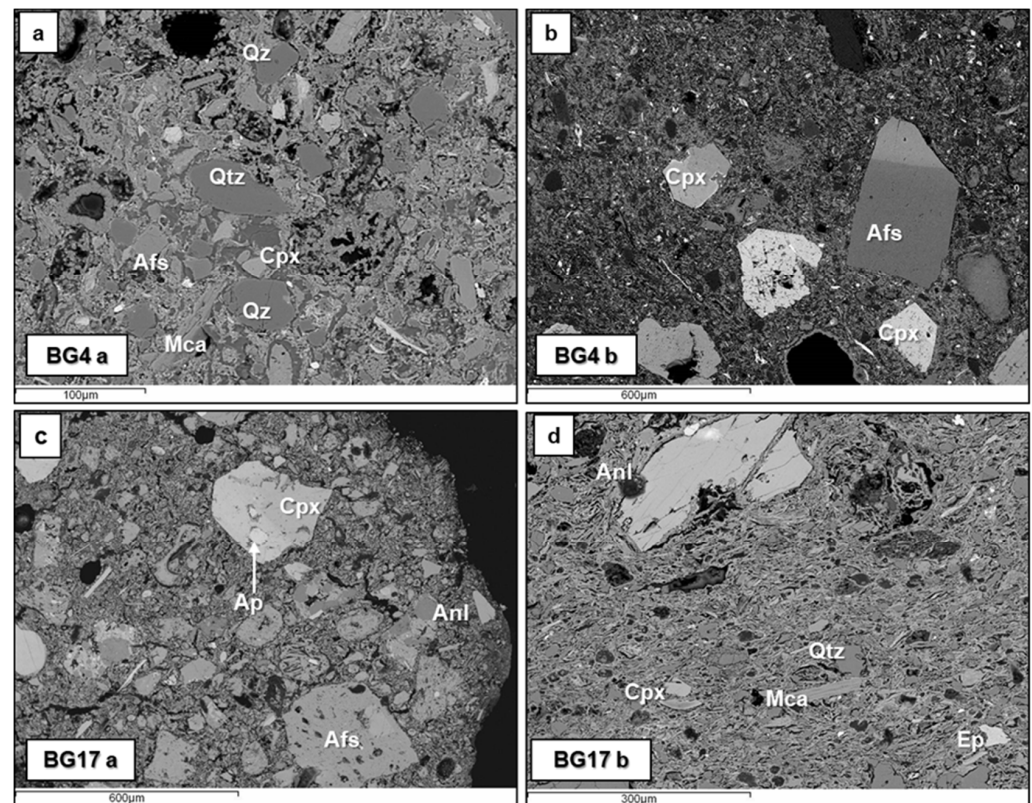


**Figure 9.** BSE-SEM images of different ceramic fragments: (a,b) BG4 sample; (c,d) BG17 sample. Abbreviations from [27], Qz quartz, Afs alkali-feldspar, Cpx clinopyroxene, Anl analcime, Mca mica, Ap apatite, Ep epidote.

**Table 7.** Average values of major oxides (wt%, recalculated to 100%, EDS) of matrix of ceramic fragments.

wt%	BG1a	BG4a	BG4b	BG7a	BG7b	BG7c	BG8a	BG8b	BG8c	BG9	BG12	BG17a	BG17b	BG17c	BG18a	BG18b	BG20
SiO <sub>2</sub>	57.68	54.18	51.00	50.00	56.07	54.07	55.58	53.90	53.84	51.36	50.94	54.31	57.63	54.94	60.57	52.53	58.77
TiO <sub>2</sub>	0.99	0.34	0.34	1.23	1.90	0.90	0.47	0.64	0.67	0.55	0.57	1.10	0.53	0.87	1.14	0.56	0.69
Al <sub>2</sub> O <sub>3</sub>	17.77	13.72	15.13	13.88	18.23	17.23	15.47	18.70	15.27	14.56	21.72	32.37	18.42	21.41	15.98	17.64	19.54
Fe <sub>2</sub> O <sub>3</sub>	7.31	4.51	4.90	-	7.11	6.11	4.64	4.79	4.43	5.11	6.09	7.08	3.90	7.57	6.32	4.29	5.49
MnO	-	-	0.18	-	0.29	0.29	0.22	-	0.10	0.11	0.20	0.17	0.58	0.03	-	0.30	0.30
MgO	5.25	5.13	3.21	2.73	5.51	3.51	2.55	2.23	2.59	3.17	10.32	5.73	2.45	4.12	3.29	3.23	2.05
* CaO	5.27	17.43	19.08	19.04	5.83	12.83	11.78	4.98	16.96	17.47	2.87	4.04	9.98	5.65	4.30	13.46	3.93
Na <sub>2</sub> O	0.18	0.45	0.66	0.12	-	-	0.14	-	-	-	-	0.07	0.14	-	-	0.09	0.23
K <sub>2</sub> O	2.79	1.04	1.65	1.91	1.22	1.22	1.95	3.06	1.58	1.80	1.32	1.23	2.76	1.21	2.00	3.50	3.50
P <sub>2</sub> O <sub>5</sub>	2.17	2.48	2.95	3.43	2.18	2.18	3.72	2.95	2.46	2.52	2.62	2.54	3.42	3.58	4.55	3.20	4.42
V <sub>2</sub> O <sub>3</sub>	0.13	0.05	0.73	0.82	1.26	1.26	0.75	0.42	0.76	0.35	0.19	0.02	-	0.11	0.63	0.66	0.95
BaO	-	0.29	-	0.11	0.39	0.39	0.20	0.61	0.20	0.16	-	0.33	-	0.41	0.11	0.38	0.13
SO <sub>3</sub>	-	-	-	2.96	-	-	2.55	2.74	1.14	2.84	3.10	-	-	-	0.97	-	-
Cl <sup>-</sup>	0.45	0.38	0.16	3.62	-	-	-	-	-	-	0.07	-	0.19	0.11	0.15	0.16	-
Total	100.00	100.00	100.00	100.00	100.00	100.00	100.00	100.00	100.00	100.00	100.00	100.00	100.00	100.00	100.00	100.00	100.00

\* CaO < 6% non calcareous clay; CaO > 6% calcareous clay.

#### 5.4. Differential Thermal and Thermogravimetric Analysis

Simultaneous thermal analyses combined with mineralogical composition of the samples allowed to obtain further information about the hydraulic characteristics of mortar samples. Table 8 reports the percentage of weight loss estimated from the TG–DTG curves within the selected temperature ranges. In the temperature range from 25 to 120 °C the weight loss is due to dehydration of hygroscopic or adsorbed water (i.e., phyllosilicates), from 120 to 200 °C the weight loss of water from hydrated salts occurs, between 200 and 600 °C the weight loss is due to structurally bound water (SBW) from the hydraulic compounds and, finally, the loss of CO<sub>2</sub> as a consequence of the decomposition of calcium carbonate (CaCO<sub>3</sub>) takes place at temperature range between 600 and 900 °C [24,46,47].

**Table 8.** TG–DTG weight losses as a function of the temperature range (wt%). Abbreviations: SBW structural boundary water, LOI loss on ignition.

Sample	Group	SBW% 200–600 °C	CO <sub>2</sub> % 600–800 °C	LOI%
BG1	C	6.30	8.43	25.89
BG3	A	5.72	6.15	27.83
BG4	B	8.60	1.023	23.69
BG6	A	8.42	13.38	37.68
BG7	B	5.21	9.08	31.00
BG8	B	7.81	9.78	37.03
BG9	C	10.13	10.12	29.33
BG10	A	4.92	8.15	17.51
BG12	A	5.70	7.97	22.68
BG13	A	4.57	8.21	23.45
BG15	A	4.75	5.64	22.06
BG18	B	4.62	8.06	20.67
BG19	B	4.50	8.49	18.27

Generally, lime mortars (or non-hydraulic mortars) are characterized by less than 3% of structural bound water (SBW) of the hydraulic components and high CO<sub>2</sub> amount (>32%), whereas mortars with higher amounts of water bound and proportionally small quantities of CO<sub>2</sub> are considered hydraulic [48].

All *Villa del Capo* mortars can be classified as hydraulic mortars, due to a weight loss at 200–600 °C (SBW values) greater of 3%, ranging from 5.64% (BG15) to 13.38 % (BG6) and CO<sub>2</sub> lower than 10 % (Table 8).

The CO<sub>2</sub> to structurally bound water ratio in relation to CO<sub>2</sub> percentage (% weight loss in the temperature range of 600–800 °C) is shown in Figure 10. The inverse trend of hydraulicity of mortars is being augmented exponentially with CO<sub>2</sub>. This representation allows a good classification of the mortar nature [24,46,48,49]. From the observation of Figure 10 and the values in Table 8 samples from *Villa del Capo* are highly hydraulic mortars and can be classified as natural pozzolanic mortars.

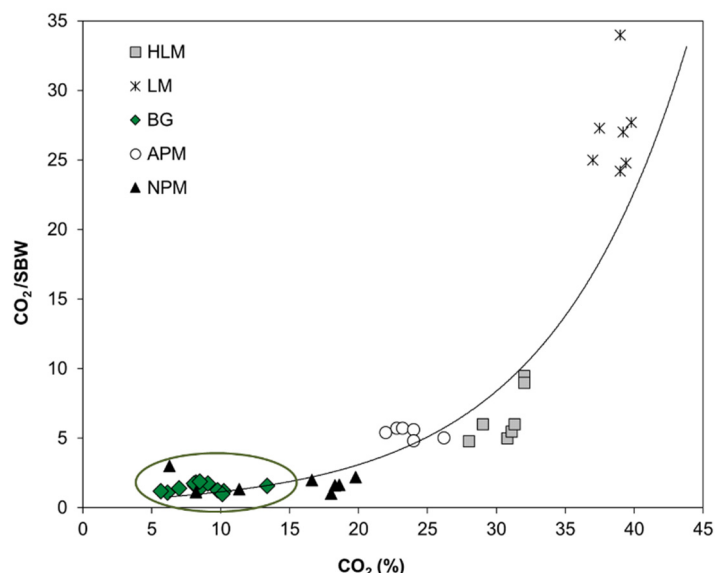


**Figure 10.** CO<sub>2</sub>/SBW vs. CO<sub>2</sub> diagram. Mortars from *Villa del Capo* (BG, green circle); NPM natural pozzolanic mortars, APM artificial pozzolanic mortars, HLM hydraulic lime mortars, and LM lime mortars from [24].

### 5.5. Porosity

Mercury intrusion porosimetry were performed on three selected samples: BG13 for Group A and BG13 and BG17 for Group B, due to the scarce amount of available material. Table 9 reports cumulative volume, bulk density, apparent density, open porosity, and specific surface, whereas Figure 11 shows representative pore size distribution.

**Table 9.** Mercury intrusion data obtained for *Villa del Capo* mortars.

Sample	BG5 (Group B)	BG13 (Group A)	BG17 (Group B)
Cumulative volume (mm <sup>3</sup> /g)	300.25	254.53	296.64
Bulk density (g/cm <sup>3</sup> )	1.51	1.38	1.57
Open porosity (Vol. %)	40.03	38.25	42.27
Specific Surface (m <sup>2</sup> /g)	32.27	30.08	34.21
Apparent Density (g/cm <sup>3</sup> )	2.71	2.57	2.89

Open porosity of BG13 sample (Group A) was slightly lower (38.25%) than BG5 and BG17 (B group; 40.03%–42.27%), all analyzed mortars show unimodal and broadened shape of cumulative pore size distribution.

Bulk densities of samples were within the range of 1.38 g/cm<sup>3</sup> to 1.57 g/cm<sup>3</sup>, whereas apparent densities were within the range of 2.57 g/cm<sup>3</sup> to 2.89 g/cm<sup>3</sup>. Relative volume curves are positively skewed and highlighted that pore radii mainly range between 5 and 100 nm. Pore sizes of samples fall within the characteristic field of hydration product porosity, usually considered below 100 nm [50,51].

Comparing these results with those obtained for modern hydraulic mortars, reported in [3], it is clearly evident that *Villa del Capo* mortars, as well as other ancient roman pozzolanic mortars of previous study [3,19], possess very small pore size radii (5–100 nm), about one order of magnitude lower than modern hydraulic mortars (100–1000 nm). These differences are probably due to the vesicular structure of pozzolanic materials (i.e., pumice) that represents a fundamental feature of the complex pore structure of the cementitious matrix of ancient mortars. Secondary minerogenetic products, in this case hydrocalumite and C-A-S-H gels, fill pores, thus enhancing bonding of pumice clasts and making mortars less permeable [36,52]. These findings (1) decrease the possibility of alteration of the mortars; (2) increase mechanical resistance, and consequently, (3) also increase durability of manufactures.

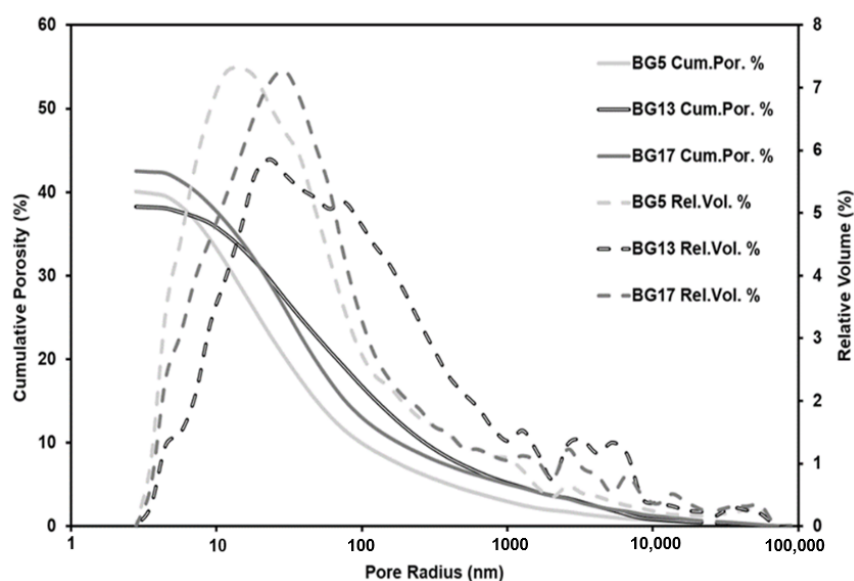


**Figure 11.** Cumulative (continuous lines) and relative (dashed lines) pore size distribution *Villa del Capo* mortars (BG5; BG13; BG17).

## 6. Conclusions

This work presents an extensive multi-analytical characterization of ancient mortars from a very important Roman archaeological site: *Villa del Capo* in the Sorrento Peninsula.

A petrographical study of the investigated samples highlighted some important aspects regarding production technology of materials, suggesting different recipes for different mortar types.

Bedding mortars result from: (1) a mixture of slaked lime, water, fine grained volcanic materials, and aggregates of volcanic rocks, whereas, coating and floor mortars may be considered as (2) a mixture of slaked lime, water, fine grained volcanic, and ceramic materials with volcanic and ceramic aggregates.

The “recipe” of coating mortars is identified as *Cocciopesto* or *Opus signinum*, a typical building technique used in ancient Rome for lining of tanks, terraces, thermal environments, and flooring [26].

Geomaterials used for mortars production had local provenance and are very well consistent with the surrounding geological setting. In fact, volcanic fragments, scoriae, pumice, and crystal fragments (i.e., clinopyroxene, feldspar, and garnet) derived from both pyroclastic rocks of the *Campi Flegrei* district and from rocks of the *Somma-Vesuvio* complex, as inferred by optical microscopy, and mineralogical and chemical composition. In coating and floor mortars (group B and C) there is an addition of ceramic fragments that improve pozzolanic aptitude of the mortar. It was not possible to define their provenance, due to strong differences among samples, which likely suggest a recycling of materials.

Provenance of carbonate rocks used to produce lime for the investigated materials is still unknown, even if it is highly reasonable to assess that they were produced “on site” from carbonate deposits of Mesozoic age that border the Campanian plain (Figure 2).

SEM-EDS analysis and TGA investigation revealed that studied mortars can be classified as hydraulic mortars, which is also confirmed by reaction rims observed around pozzolanic materials.

XRPD and SEM-EDS analysis highlighted that binder fractions are characterized by different secondary products (reaction products), including amorphous C-A-S-H gel, calcite, gypsum, and hydrocalumite.

Results of porosity tests together with microstructural observations suggest the products related to minerogenetic secondary processes, especially gel C-A-S-H and hydrocalumite settling in the porous of pozzolanic materials, make mortars more resistant.

Studies like this, that entail meticulous characterization of all the components for the realization of the artificial geomaterials, paying special attention to secondary minerogenetic processes, are crucial in the perspective of future restoration works, and especially for the preservation of archaeological sites that cannot be independent from thorough knowledge of materials used for the construction and of their state of conservation, along with that of the building.

**Supplementary Materials:** The following are available online at <https://www.mdpi.com/article/10.3390/min11050469/s1>, Table S1: Major element concentrations of pumice fragments (wt%, recalculated to 100%, EDS). Na<sub>2</sub>O + K<sub>2</sub>O also shown; Table S2: Representative chemical composition (wt%, EDS) of garnets.

**Author Contributions:** Sampling, C.R. and R.E.; archaeological information, R.E.; formal analysis and data curation, C.R., L.G. and P.C.; writing—original draft preparation, C.R.; writing—review & editing, C.R., L.G. and P.C.; supervision, P.C. All authors have read and agreed to the published version of the manuscript.

**Funding:** This research received no external funding.

**Data Availability Statement:** All data derived from this research are presented in the enclosed figures and tables.

**Acknowledgments:** This paper stem from the doctoral thesis of one of the Authors (CR) in earth science, environment, and resources at DiSTAR of Federico II University of Naples. The analysis of

additional samples was supported by the following AIM projects [AIM18352321–1; AIM1835232–1, CUP: E66C18001140005]. The authors would like to thank Roberto de Gennaro for the invaluable assistance during EDS microanalyses, Sergio Bravi for his technical ability in thin sections preparation and Tommasina Budetta, former *Sovrintendenza archeologia della Campania* that provided authorization and useful support on sampling. Thanks, are also due to CTG Italcementi Heidelberg Group for supporting this research activity. The authors would like to thank the journal editors and the anonymous reviewers for their useful comments that helped us in the revision of this manuscript.

**Conflicts of Interest:** The authors declare no conflict of interest.

## References

1. D'Arms, J.H. Romans on the Bay of Naples. A Social and Cultural Study of the Villas and their Owners from 150 B.C. to A.D. 400. In *Romans on the Bay of Naples and Other Essays on Roman Campania*; Zevi, F., Ed.; Edipuglia: Bari, Italy, 2003; pp. 1–226.
2. Filser, W.; Fritsch, B.; Kennedy, W.; Klose, C.; Perrella, R. Surrounded by the Sea: Re-Investigating the Villa Maritima Del Capo Di Sorrento. *J. Roman Archaeol.* **2017**, *30*. [[CrossRef](#)]
3. Rispoli, C.; de Bonis, A.; Esposito, R.; Graziano, S.F.; Langella, A.; Mercurio, M.; Morra, V.; Cappelletti, P. Unveiling the Secrets of Roman Craftsmanship: Mortars from Piscina Mirabilis (Campi Flegrei, Italy). *Archaeol. Anthropol. Sci.* **2020**, *12*. [[CrossRef](#)]
4. Graziano, S.F.; Rispoli, C.; Guarino, V.; Balassone, G.; di Maio, G.; Pappalardo, L.; Cappelletti, P.; Damato, G.; de Bonis, A.; di Benedetto, C.; et al. The roman villa of positano (Campania region, Southern Italy): Plasters, tiles and geoarchaeological reconstruction. *Int. J. Conserv. Sci.* **2020**, *11*, 319–344.
5. Izzo, F.; Arizzi, A.; Cappelletti, P.; Cultrone, G.; de Bonis, A.; Germinario, C.; Graziano, S.F.; Grifa, C.; Guarino, V.; Mercurio, M.; et al. The Art of Building in the Roman Period (89 B.C.-79 A.D.): Mortars, Plasters and Mosaic Floors from Ancient Stabiae (Naples, Italy). *Constr. Build. Mater.* **2016**, *117*, 129–143. [[CrossRef](#)]
6. De Bonis, A.; Grifa, C.; Langella, A.; Mercurio, M.; Luisa Perrone, M.; Morra, V. Archaeometric Study of Roman Pottery from Caudium Area (Southern Italy). *Period. Mineral.* **2011**, *79*, 73–89.
7. Guarino, V.; de Bonis, A.; Grifa, C.; Langella, A.; Morra, V.; Pedroni, L. Archaeometric Study on Terra Sigillata from Cales (Italy). *Period. Mineral.* **2011**, *80*, 455–470. [[CrossRef](#)]
8. Rispoli, C. Ancient Roman Mortars: Mix Design, Mineralogical Composition and Minerogenetic Secondary Processes. Ph.D. Thesis, Federico II University of Naples, Naples, Italy, 2017.
9. Cinque, A.; Robustelli, G. Alluvial and Coastal Hazards Caused by Long-Range Effects of Plinian Eruptions: The Case of the Lattari Mts. After the AD 79 Eruption of Vesuvius. *Geol. Soc. Spec. Publ.* **2009**, *322*, 155–171. [[CrossRef](#)]
10. Aucelli, P.; Cinque, A.; Mattei, G.; Pappone, G. Historical Sea Level Changes and Effects on the Coasts of Sorrento Peninsula (Gulf of Naples): New Constrains from Recent Geoarchaeological Investigations. *Palaeogeogr. Palaeoclimatol. Palaeoecol.* **2016**, *463*, 112–125. [[CrossRef](#)]
11. Brancaccio, L.; Cinque, A.; Romano, P.; Roskopf, C.; Russo, F.; Santo, A.; Santangelo, N. Geomorphology and Neotectonic Evolution of a Sector of the Tyrrhenian Flank of the Southern Apennines, (Region of Naples, Italy). *Z. Geomorphol.* **1991**, *82*, 47–58.
12. Iannace, A.; Merola, D.; Perrone, V.; Amato, A.; Cinque, A.; Santacroce, R.; Sbrana, A.; Sulpizio, R.; Budillon, F.; Conforti, A.; et al. *Note Illustrative Della Carta Geologica d'Italia Alla Scala 1: 50.000 Fogli 466–485 Sorrento-Termini*; Servizio Geologico d'Italia: Ispra, Italy, 2015.
13. Santacroce, R.; Cioni, R.; Marianelli, P.; Sbrana, A.; Sulpizio, R.; Zanchetta, G.; Donahue, D.J.; Joron, J.L. Age and Whole Rock-Glass Compositions of Proximal Pyroclastics from the Major Explosive Eruptions of Somma-Vesuvius: A Review as a Tool for Distal Tephrostratigraphy. *J. Volcanol. Geotherm. Res.* **2008**, *177*, 1–18. [[CrossRef](#)]
14. Vitale, S.; Tramparulo, F.D.; Ciarcia, S.; Amore, F.O.; Prinzi, E.P.; Laiena, F. The Northward Tectonic Transport in the Southern Apennines: Examples from the Capri Island and Western Sorrento Peninsula (Italy). *Int. J. Earth Sci.* **2017**, *106*, 97–113. [[CrossRef](#)]
15. Mingazzini, P. *Forma Italiae: Latium et Campania*; De Luca Ed: Surrentum, Italy, 1946.
16. Budetta, T.; de Martino, R.; Franchino, R.; Frettoloso, C. The System of Environmental Networks for the Use of Archaeological Sites in Areas of Natural Beauty. *J. Sustain. Archit. Civ. Eng.* **2013**, *3*. [[CrossRef](#)]
17. Howarth, J. Improved Estimators of Uncertainty in Proportions, Point-Counting, and Pass-Fail Test Results. *Am. J. Sci.* **1998**, *298*, 594–607. [[CrossRef](#)]
18. Pouchou, J.L.; Pichoir, F. A simplified version of the PAP model for matrix corrections in EPMA. In *Microbeam Analysis*; San Francisco Press: San Francisco, CA, USA, 1988.
19. Rispoli, C.; De Bonis, A.; Guarino, V.; Graziano, S.F.; di Benedetto, C.; Esposito, R.; Morra, V.; Cappelletti, P. The Ancient Pozzolan Mortars of the Thermal Complex of Baia (Campi Flegrei, Italy). *J. Cult. Herit.* **2019**, *40*. [[CrossRef](#)]
20. ASTM D4404–10. *Standard Test Method for Determination of Pore Volume and Pore Volume Distribution of Soil and Rock by Mercury Intrusion Porosimetry*; STM International: West Conshohocken, PA, USA, 2010.
21. Wentworth, C.K. A Scale of Grade and Class Terms for Clastic Sediments. *J. Geol.* **1922**, *30*, 377–392. [[CrossRef](#)]
22. Addis, A.; Secco, M.; Marzaioli, F.; Artioli, G.; Chavarría Arnau, A.; Passariello, I.; Terrasi, F.; Brogiolo, G.P. Selecting the Most Reliable <sup>14</sup>C Dating Material inside Mortars: The Origin of the Padua Cathedral. *Radiocarbon* **2019**, *61*, 375–393. [[CrossRef](#)]

23. Ricca, M.; Galli, G.; Ruffolo, S.A.; Sacco, A.; Aquino, M.; la Russa, M.F. An Archaeometric Approach of Historical Mortars Taken from Foligno City (Umbria, Italy): News Insight of Roman Empire in Italy. *Archaeol. Anthropol. Sci.* **2019**, *11*, 2649–2657. [[CrossRef](#)]
24. Moropoulou, A.; Bakolas, A.; Anagnostopoulou, S. Composite Materials in Ancient Structures. *Cement Concr. Compos.* **2005**, *27*, 295–300. [[CrossRef](#)]
25. Colella, A.; Di Benedetto, C.; Calcaterra, D.; Cappelletti, P.; D'Amore, M.; Di Martire, D.; Graziano, S.F.; Papa, L.; de Gennaro, M.; Langella, A. The Neapolitan Yellow Tuff: An Outstanding Example of Heterogeneity. *Constr. Build. Mater.* **2017**, *136*, 361–373. [[CrossRef](#)]
26. Collepardi, M.; Collepardi, S.; Troli, R. *Il Nuovo Calcestruzzo*, 5th ed.; Tintoretto: Treviso, Italy, 2009.
27. Whitney, D.L.; Evans, B.W. Abbreviations for Names of Rock-Forming Minerals. *Am. Miner.* **2010**, *95*, 185–187. [[CrossRef](#)]
28. UNI-EN 11305:2009. *Norme tecniche per i Beni Culturali. Malte Storiche: Linee Guida per La Caratterizzazione Mineralogico Petrografica, Fisica e Chimica Delle Malte*; CNR-ICR: Roma, Italy, 2009.
29. De Gennaro, M.; Colella, C.; Pansini, M. Hydrothermal Conversion of Trachytic Glass into Zeolite. II Reactions with High-Salinity Waters. *Neues Jahrb. Mineral. Mon.* **1993**, *3*, 97–110.
30. Tian, J.; Guo, Q. Thermal Decomposition of Hydrocalumite over a Temperature Range of 400–1500 °C and Its Structure Reconstruction in Water. *J. Chem.* **2014**, *2014*. [[CrossRef](#)]
31. Wei, G.; Germinario, C.; Grifa, C.; Ma, X. Characterization of Ancient Building Lime Mortars of Anhui Province, China: A Multi-Analytical Approach. *Archaeometry* **2020**, *62*, 888–903. [[CrossRef](#)]
32. Kalinichev, A.G.; Kirkpatrick, R.J.; Cygan, R.T. Molecular Modeling of the Structure and Dynamics of the Interlayer and Surface Species of Mixed-Metal Layered Hydroxides: Chloride and Water in Hydrocalumite (Friedel's Salt). *Am. Mineral.* **2000**, *85*. [[CrossRef](#)]
33. De Gennaro, M.; Incoronato, A.; Mastrolorenzo, G.; Adabbo, M.; Spina, G. Depositional Mechanisms and Alteration Processes in Different Types of Pyroclastic Deposits from Campi Flegrei Volcanic Field (Southern Italy). *J. Volcanol. Geotherm. Res.* **1999**, *91*, 303–320. [[CrossRef](#)]
34. Langella, A.; Bish, D.L.; Cappelletti, P.; Cerri, G.; Colella, A.; de Gennaro, R.; Graziano, S.F.; Perrotta, A.; Scarpati, C.; de Gennaro, M. New Insights into the Mineralogical Facies Distribution of Campanian Ignimbrite, a Relevant Italian Industrial Material. *Appl. Clay Sci.* **2013**, *72*, 55–73. [[CrossRef](#)]
35. Moropoulou, A.; Cakmak, A.; Labropoulos, K.C.; van Grieken, R.; Torfs, K. Accelerated Microstructural Evolution of a Calcium-Silicate-Hydrate (C-S-H) Phase in Pozzolanic Pastes Using Fine Siliceous Sources: Comparison with Historic Pozzolanic Mortars. *Cem. Concr. Res.* **2004**, *34*, 1–6. [[CrossRef](#)]
36. Jackson, M.D.; Mulcahy, S.R.; Chen, H.; Li, Y.; Li, Q.; Cappelletti, P.; Wenk, H.R. Phillipsite and Al-Tobermorite Mineral Cements Produced through Low-Temperature Water-Rock Reactions in Roman Marine Concrete. *Am. Mineral.* **2017**, *102*, 1435–1450. [[CrossRef](#)]
37. Boynton, R.S. *Chemistry and Technology of Lime and Limestone*; Sons, J.W., Ed.; Interscience: New York, NY, USA, 1996.
38. De Luca, R.; Miriello, D.; Pecci, A.; Domínguez-Bella, S.; Bernal-Casasola, D.; Cottica, D.; Bloise, A.; Crisci, G.M. Archaeometric Study of Mortars from the Garum Shop at Pompeii, Campania, Italy. *Geoarchaeology* **2015**, *30*, 330–351. [[CrossRef](#)]
39. Columbu, S.; Sitzia, F.; Ennas, G. The Ancient Pozzolanic Mortars and Concretes of Heliocaminus Baths in Hadrian's Villa (Tivoli, Italy). *Archaeol. Anthropol. Sci.* **2017**, *9*, 523–553. [[CrossRef](#)]
40. Le Bas, M.J.; Le Maitre, R.W.; Streckeisen, A.; Zanettin, B. A Chemical Classification of Volcanic Rocks Based on the Total Alkali-Silica Diagram. *J. Petrol.* **1986**, *27*, 745–750. [[CrossRef](#)]
41. Locock, A.J. An Excel Spreadsheet to Recast Analyses of Garnet into End-Member Components, and a Synopsis of the Crystal Chemistry of Natural Silicate Garnets. *Comput. Geosci.* **2008**, *34*, 1769–1780. [[CrossRef](#)]
42. Scheibner, B.; Wörner, G.; Civetta, L.; Stosch, H.G.; Simon, K.; Kronz, A. Rare Earth Element Fractionation in Magmatic Ca-Rich Garnets. *Contrib. Mineral. Petrol.* **2007**, *154*, 55–74. [[CrossRef](#)]
43. Morra, V.; Calcaterra, D.; Cappelletti, P.; Colella, A.; Fedele, L.; de Gennaro, R.; Langella, A.; Mercurio, M.; de Gennaro, M. Urban Geology: Relationships between Geological Setting and Architectural Heritage of the Neapolitan Area. *J. Virtual Explor.* **2010**, *36*. [[CrossRef](#)]
44. Maniatis, M.S.; Tite, Y. Technological Examination of Neolithic-Bronze Age Pottery from Central and Southeast Europe and from the Near East. *J. Archaeol. Sci.* **1981**, *8*, 59–76. [[CrossRef](#)]
45. De Bonis, A.; Cultrone, G.; Grifa, C.; Langella, A.; Morra, V. Clays from the Bay of Naples (Italy): New Insight on Ancient and Traditional Ceramics. *J. Eur. Ceram. Soc.* **2014**, *34*, 3229–3244. [[CrossRef](#)]
46. Genestar, C.; Pons, C.; Más, A. Analytical characterisation of ancient mortars from the archaeological Roman city of pollentia (Balearic Islands, Spain). *Anal. Chim. Acta* **2006**, *557*, 373–379. [[CrossRef](#)]
47. Izzo, F.; Grifa, C.; Germinario, C.; Mercurio, M.; de Bonis, A.; Tomay, L.; Langella, A. Production Technology of Mortar-Based Building Materials from the Arch of Trajan and the Roman Theatre in Benevento, Italy. *Eur. Phys. J. Plus* **2018**, *133*. [[CrossRef](#)]
48. Borsoi, G.; Santos Silva, A.; Menezes, P.; Candeias, A.; Mirão, J. Analytical Characterization of Ancient Mortars from the Archaeological Roman Site of Pisões (Beja, Portugal). *Constr. Build. Mater.* **2019**, *204*, 597–608. [[CrossRef](#)]
49. Moropoulou, A.; Bakolas, A.; Aggelakopoulou, E. Evaluation of Pozzolanic Activity of Natural and Artificial Pozzolans by Thermal Analysis. *Thermochim. Acta* **2004**, *420*, 135–140. [[CrossRef](#)]

- 
50. Mehta, K.P.; Monteiro, P.J.M. *Concrete: Microstructure, Properties, and Materials*, 4th ed.; McGraw-Hill Education: London, UK, 2014.
  51. Gotti, E.; Oleson, J.P.; Bottalico, L.; Brandon, C.; Cucitore, R.; Hohlfelder, R.L. A Comparison of the Chemical and Engineering Characteristics of Ancient Roman Hydraulic Concrete with a Modern Reproduction of Vitruvian Hydraulic Concrete. *Archaeometry* **2008**, *50*, 576–590. [[CrossRef](#)]
  52. Brandon, C.J.; Hohlfelder, R.L.; Jackson, M.D.; Oleson, J.P. Building for eternity. In *The History and Technology of Roman Concrete Engineering in the Sea*; Oxbow Books: Oxford, UK, 2014; Volume 53, ISBN 9788578110796.